Langmuir

ARTICLE

pubs.acs.org/Langmuir

Distinct Conformations of DNA-Stabilized Fluorescent Silver Nanoclusters Revealed by Electrophoretic Mobility and Diffusivity Measurements

Til Driehorst,[†,⊥] Patrick O'Neill,[‡] Peter M. Goodwin,[§] Sumita Pennathur,[†] and D. Kuchnir Fygenson*[,‡,∥]

[†]Mechanical Engineering Department, [‡]Physics Department, and [∥]Biomolecular Science & Engineering Program, University of California, Santa Barbara, California, United States

[§]Center for Integrated Nanotechnologies, Los Alamos National Laboratory, Los Alamos, New Mexico, United States

Supporting Information

ABSTRACT: Silver−DNA nanoclusters (Ag:DNAs) are novel fluorophores under active research and development as alternative biomolecular markers. Comprised of a few-atom Ag cluster that is stabilized in water by binding to a strand of DNA, they are also interesting for fundamental explorations into the properties of metal molecules. Here, we use in situ calibrated electrokinetic microfluidics and fluorescence correlation spectroscopy to determine the size, charge, and conformation of a select set of Ag:DNAs. Among them is a pair of spectrally distinct Ag:DNAs stabilized by the same DNA sequence, for which it is known that the silver cluster differs by two atoms. We find these two Ag:DNAs differ in size by ∼30%, even though their molecular weights differ by less than 3%. Thus a single DNA sequence can adopt very different conformations when binding slightly different Ag clusters. By comparing spectrally identical Ag:DNAs that differ in sequence, we show that the more compact conformation is insensitive to the native DNA secondary structure. These results demonstrate electrokinetic microfluidics as a practical tool for characterizing Ag:DNA.

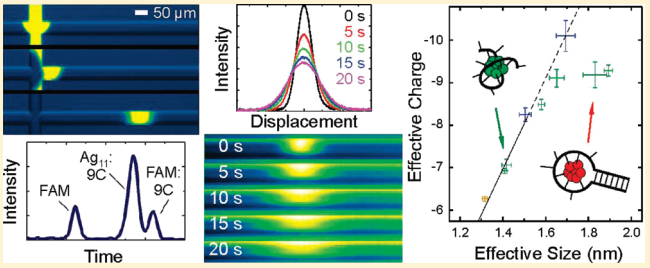

INTRODUCTION

The utility of fluorescence has exploded over the past two decades. A plethora of novel imaging,[1] characterization[2] and separation technologies[3] has emerged, enabled in part by the diversity of available fluorophores. Applications that push the limits of these technologies, in turn, motivate the development of new fluorophores. Organic dyes,[4] fluorescent proteins,[5] colloidal quantum dots,[6] and, most recently, few-atom noble metal clusters[7] have each proven useful for specific applications. Noble metal clusters are of increasing interest not only for their photophysical properties—in certain applications they offer improved brightness and photostability compared to organic dyes[8]—but also because their composition invites physical modeling, raising prospects for the rational design of key properties.[9]

In 2004, Dickson and colleagues showed that DNA can stabilize fluorescent few-atom Ag clusters (Ag:DNAs) in aqueous solution.[10] Since then, Ag:DNAs have been used as biological labels,[11] for detection of other metal ions,[12] and to enable a new microscopy technique that exploits their optically addressable dark states for high-resolution, low-background imaging.[13] Their fluorescence spectra and quantum yields, as well as chemical- and photostability, depend on the type, number, and sequence of the bases in the DNA strand.[9,14−16] To date, the use of different sequences has uncovered Ag:DNAs with emission ranging from the blue to the near-infrared[9] and fluorescence quantum yields as high as 64%.[16] DNA sequence is thus a powerful parameter in the design of Ag-cluster fluorophores, dramatically altering excitation and emission spectra with potentially little or no change in other distinguishing characteristics such as size or charge state. A more detailed structural understanding of the Ag:DNA complex, however, is needed to enable physical modeling and direct engineering.

What little structural information there is about Ag:DNA has come primarily from mass spectrometry[15] and size exclusion chromatography.[17] High-resolution techniques, such as crystallography or NMR, await improved synthesis protocols that yield greater concentrations of chemically pure emitters. Until these materialize, fluorescence-based techniques are probably the best means for extracting species-specific structural constraints.

In this paper, we derive structural insight into a select few Ag:DNA nanoclusters using primarily electrokinetic microfluidic characterization. Microfluidic electrophoresis readily provides information on relative electrophoretic mobility, but absolute measurements require thorough and frequent characterization of the microfluidic channels.[18] We begin by experimentally validating a technique for the in situ measurement of channel properties and proceed to measure electrophoretic mobility with an accuracy of

Received: March 4, 2011
Revised: May 7, 2011
Published: June 17, 2011

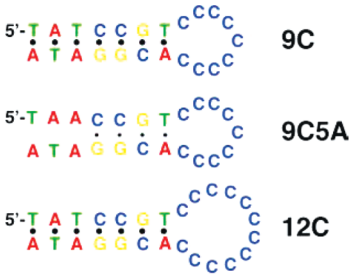

Figure 1. DNA sequences used in this study. 9C is designed to support a simple hairpin conformation, with a blunt-ended double-stranded 7 bp (base-pair) stem clamping a single-stranded loop of nine cytosines. 9C5A is identical to 9C except for an A-A mismatch 5 bp from the loop, which is predicted to destabilize the stem.[21] 12C is identical to 9C except for three additional cytosines in the loop. A fluorescein (FAM) label, when present, is covalently linked to the 5′ terminus and adds negative charge. Silver atom clusters, when present, are expected to bind loop cytosines but may bind elsewhere, as well. Hence, the DNA conformation in the presence of silver is unknown.

$\pm 3.5\%$ and a precision of $\leq \pm 10^{-9}$ m^2 V^{-1} s^{-1}. Microfluidics also enable the simple and accurate measurement of diffusivity. We demonstrate consistency between diffusivity measurements made by the "static" microfluidic technique[19] and by fluorescence correlation spectroscopy (FCS)[20] and resort to FCS to measure the diffusivity of one Ag:DNA whose poor photostability precluded microfluidic measurement. Finally, on the basis of diffusivity and electrophoretic mobility measurements and a comparison of fluorescence spectra from silver-cluster fluorophores housed in different DNA sequences, we draw conclusions about the size, charge, and conformation of our Ag:DNA nanoclusters.

Our focus is on two spectrally distinct Ag:DNAs for which the number of Ag atoms in the cluster is known.[15] These share a common DNA sequence that can adopt a hairpin structure in which the single-stranded loop is comprised only of cytosines (Figure 1). We ask whether silver atom number is the primary difference between these fluorophores or whether they also differ significantly in structure and charge state. We modify the sequence to generate spectrally similar Ag:DNAs and determine their mobility and diffusivity as well, together with those of a subset of the DNA sequences without Ag. By comparing our independent measurements of electrophoretic mobility and diffusivity among these analytes, and in as many as three different buffer conditions (pH 4.8, 7.0, 9.2), we conclude that a major structural change, and not just a difference in atom number, is responsible for the spectral difference between the two Ag:DNAs of common sequence.

EXPERIMENTAL SECTION

Ag:DNA. DNA oligomers were purchased with standard desalting from Integrated DNA Technologies. Their base sequences were designed to support a hairpin structure with a single stranded loop of cytosines clamped by a 7 bp stem (Figure 1). It is known, however, that Ag^+ can mediate non-Watson−Crick base pairing, especially between cytosines.[22,23] The structure of the oligomers when part of a Ag:DNA complex is thus not necessarily a hairpin.

We refer to the oligomers as "9C" (6866 g/mol) and "12C" (7733 g/mol), in accordance with their sequence: 5′-TATCCGT-C_m-ACGGATA-3′, where m = 9 or 12, respectively. To test the relevance of the hairpin structure, we used a variant of the 9C sequence, "9C5A" (6875 g/mol): 5′-TAACCGT-C_9-ACGGATA-3′, which has a mismatch that is predicted to destabilize Watson−Crick base pairing in the stem.[21] To test the relevance of the intact stem sequence, we used three more variants of the 9C sequence: "9Cstem2×", 5′-ATTGCAGTATCCGT-C_9-ACGGATACTG-CAAT-3′, which has twice as many base pairs stabilizing the hairpin; "9CstemAT", 5′-TATTAAT-C_9-ATTAATA-3′, which has a cytosine-free stem; and "9Cstem26", 5′-TGTCCAT-C_9-ATGGACA-3′, which has the same base pairs in the stem, but in a slightly different order.

Fluorescent Ag:DNAs were synthesized by mixing $AgNO_3$ with DNA in buffer, incubating at room temperature for about 30 min, then adding $NaBH_4$ and storing at 4 °C until use. Three different buffers were used for microfluidic measurements: sodium acetate ($C_2H_3NaO_2$) at pH 4.8, sodium phosphate (NaH_2PO_4) at pH 7.0, and sodium borate ($Na_2[B_4O_5(OH)_4]$) at pH 9.2. The final mixtures contained 10 mM buffer, 25 μM DNA, 200 μM $AgNO_3$, and 100 μM $NaBH_4$. FCS and fluorometry measurements were both performed on solutions prepared with 25 μM DNA, 40 mM ammonium acetate at pH 7.0, 150 μM $AgNO_3$, 50 μM $NaBH_4$.

We refer to the resulting fluorophores as "Ag_n:mC", where n is the number of silver atoms in the cluster,[15] m is the number of cytosines in the loop, and the variant sequences are denoted by additional alphanumerics (5A, stem2×, stemAT, stem26). Measurements were also made on DNA sequences 9C and 9C5A without Ag, in which case the oligomer was purchased with a fluorescein label (FAM) covalently linked to the 5′ end. These we refer to as FAM:9C and FAM:9C5A.

Fluorescence spectra are provided in the Supporting Information.

Microfluidic Device and Setup. Microchannel devices were designed and custom fabricated in fused-silica wafers using conventional MEMS processing techniques (Domolite, Inc.). The devices had a simple cross channel geometry with four inlet/outlet ports (Figure 2). Channel dimensions were 20 μm deep by 50 μm wide for all measurements but one, in which a channel 1 μm deep by 9 μm wide was used and yielded the same results as the larger channel. To minimize adsorption and inhibit dissolution of the channel surface, a coating of neutral silane was applied by filling the channels with a ∼100 mM solution of 3-cyanopropyldimethylchlorosilane in acetonitrile and incubating for 12 h at room temperature.[24,25] The channels were then rinsed with and immersed in ethanol to preserve the coating during storage.

In preparation for use, liquid reservoirs made from polystyrene pipet tips cut with a razor blade (∼55 μL) were press-fit into to the chip reservoirs. Increasing the reservoir volume minimized pH-gradients along the channel that can result from electrochemistry at the electrodes.[26] It also prevented mechanical contact between the electrodes and the chip, which can result in flakes from the electrode tip that clog the channel. Once the reservoirs were attached, the ethanol-filled device was connected to the experimental setup (Figure 2) and flushed electrokinetically (see below) with buffer until the electric current stabilized. Care was taken during buffer exchanges and sample introduction to avoid introducing bubbles or particulate matter into the channels. All solutions were filtered with 0.2 μm PTFE syringe filters prior to use. After use, channels were rinsed with water. Between experiments channels were stored in ethanol.[27]

Fluorescence Imaging. The motion and spatial distribution of analytes in the channel were imaged with an epifluorescence inverted microscope (Olympus IX70) fitted with a 20×/0.75NA objective lens (UPlsApo, Olympus) and a 0.5× demagnifier, to maximize sensitivity while maintaining a large field of view (Figure 2). Fluorescence was excited using a 200 W Hg arc lamp. Interference filters and a dichroic mirror appropriate for the fluorophore of interest were used to separate the fluorescence emission from the excitation. For Ag_{11}:9C, Ag_{11}:9C5A, FAM:9C, and FAM:9C5A, the excitation filter was a 20 nm band-pass centered at 410 nm (Chroma D410/20X), the emission filter was a 50 nm band-pass centered at 520 nm (Chroma HQ520/50M), and the dichroic was a 475 nm long-pass (Omega XF2007). For Ag_{13}:9C and Ag_n:12C, the excitation filter was a 12 nm band-pass centered at 546 nm (Chroma HQ546/12X), the emission filter was a 30 nm band-pass

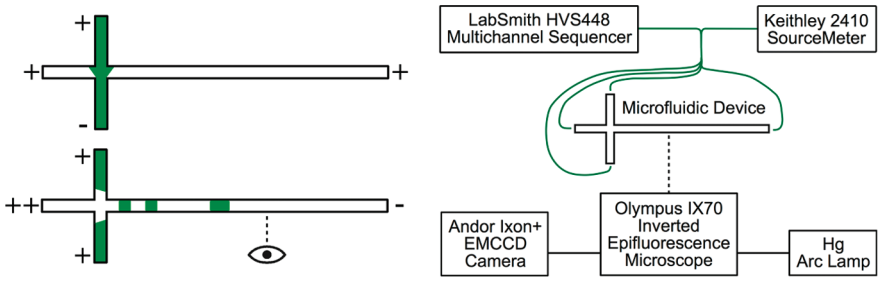

Figure 2. Experiment setup. (Left) Schematic of the microfluidic device. Top and bottom depict loading and injection, respectively. (Right) Schematic of experimental setup. Motion and spatial distribution of fluorophores in the microfluidic device were imaged with an inverted epifluorescence microscope equipped with a Hg arc lamp. Images were recorded digitally via an EMCCD camera. Voltages were applied via platinum wire electrodes in polystyrene liquid reservoirs using a multichannel, high-voltage sequencer (for injection experiments) or a digital sourcemeter (for current monitoring).

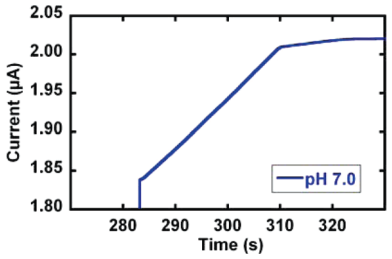

Figure 3. Raw data from current monitoring for a channel initially filled with 9 mM sodium phosphate buffer at pH 7.0 and abruptly switched to a target concentration of 10 mM. Current increases steadily as buffer at the target concentration migrates through the eastern channel (Figure 2) and the slope changes abruptly once it reaches the intersection. The duration of this transient divided by the channel length is a direct measure of the electroosmotic velocity and thus the ζ-potential. In this case, the electric field in the eastern channel was 16.5 kV/m.

centered at 630 nm (Omega XF3028), and the dichroic was a 590 nm long-pass (Omega XF2019).

Images were recorded using a cooled, backlit, and intensified EMCCD videocamera (Ixon+, Andor Co.) with a 512 × 512 pixel array and 12-bit digitization to a PC. The exposure time was 100 ms and the frame rate was 10 Hz, except when measuring fluorescein alone (50 ms, 20 Hz) or when testing for possible photobleaching during diffusivity measurements. On-chip 1 × 4 binning perpendicular to the channel axis was used to increase the signal-to-noise ratio (SNR) when the injected plug volume was small or the analyte was dim. During diffusivity measurements, a signal from the camera controller actuated a shutter (Uniblitz VS35, Vincent Associates) in the illumination path to minimize photobleaching. Background subtraction as well as normalization were performed on all diffusivity images using the free software NIH ImageJ.[28]

Current Monitoring. ζ-Potential was measured by current monitoring (CM) as described in detail elsewhere,[29] with some modification to accommodate the cross-channel geometry. First, as in typical CM experiments, one reservoir was filled with a background electrolyte (BGE) whose concentration was 90% of the target BGE concentration. Then, voltages were applied to the four wells (north, west, and south being at ground, east at high) to generate constant electroosmotic flow from the east. Electric fields were generated across the microfluidic channel by applying voltages from a high-voltage sourcemeter (model 2410, Keithley) to platinum wire electrodes placed within each fluid reservoir of the device. Three different electric field strengths in the eastern channel were used: 9.9, 12.2, and 16.5 kV/m. After applying voltages, the system was allowed to equilibrate for about 15 min. Finally, all liquid was removed from the eastern well and replaced with BGE at the target concentration, and the current was monitored over time (Figure 3).

As the BGE of higher concentration enters the channel and migrates from the eastern well toward the intersection, the current increases at a constant rate. Once it reaches the intersection, the slope changes abruptly. The length of the eastern arm divided by the duration of this initial transient is a direct measurement of area-averaged velocity. In microchannels with a thin electric double layer (EDL), the relation between area-averaged velocity, applied electric field, and ζ-potential is given by the Helmholtz−Smoluchowski equation.[30] ζ-potential is a property of the substrate/electrolyte interface that depends on the details of substrate composition, local ionic concentration, and pH. It is thus neither predictable from first principles nor amenable to one-off calibration, because it changes as the channel is exposed to analyte, cleaned, and re-exposed.[30,31] CM was therefore performed in all three buffers and each CM was immediately followed by injection experiments (see below) to characterize the electrophoretic mobility of a reference dye, fluorescein. Fluorescein was thereafter used as a reference plug in all injection experiments of DNA-fluorophores as an in situ ζ-potential calibration.

Electrophoretic Mobility and Diffusivity Measurements via Electrokinetic Microfluidics. Electrophoretic mobility was determined directly from time-to-arrival measurements following electrokinetic injections, as described by Pennathur et al.[32] Electric fields were generated across the microfluidic channels by applying voltages from a multichannel, high-voltage sequencer (HVS448-6000D, Labsmith Inc.) to platinum wire electrodes placed within each fluid reservoir of the device. A preprogrammed sequence of voltages established the desired fields for sample loading, injection, and flushing following the method of Bharadwaj et al.[33] Briefly, for loading, the sample solution was placed in the northern well and electrodes in the northern, western, and eastern wells were set to positive voltages while the southern well was grounded, resulting in electrokinetic flow from all wells to the south. For injection, the applied voltages were then switched so that the western well was positive, northern and southern wells were less so, and the eastern well was grounded. This resulted in a plugwise injection into the eastern channel (Figure 2). We used two different voltage schemes for the injection step, with electric fields of 9.0 and 13.5 kV/m along the eastern channel. For analytes with low signal-to-noise ratio, we introduced a loading step with electric fields different from those proposed by Bharadwaj et al. We lowered the electric fields in the eastern and western channel relative to that in the northern channel, thereby broadening the initial plug and increasing the resulting signal. Between injections, the channel was flushed by applying a voltage scheme similar to that used in the loading step, but with lower electric fields to retard electrochemistry at the electrodes. Electrochemistry at the electrodes eventually creates pH-gradients within the channel, which result in internal pressure gradients and thereby decrease the reproducibility and accuracy of results and increase the dispersion of the analyte plug.[26]

The microscope objective was positioned downstream of the injection point and the time required for the analyte to reach the center of the

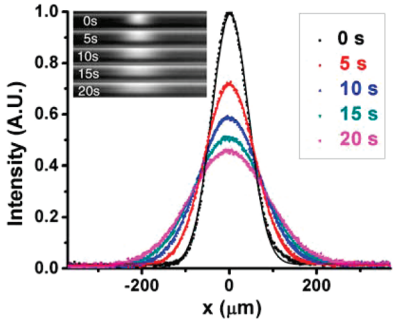

Figure 4. Diffusivity measurements of Ag_{11}:9C at pH 7.0. The Gaussian band broadening is monitored under static conditions. The time-evolution of the widths of the Gaussians yields the molecular diffusion constant D of the species of interest.

field of view was measured. Next, the electroosmotic velocity was subtracted from the measured velocity to give the electrophoretic velocity of the analyte. The electroosmotic velocity, u_{EOF}, was calculated using the measured ζ-potential via the Helmholtz−Smoluchowski equation, $u_{EOF} = \varepsilon E\zeta/\mu$, where ε is the dielectric constant of the buffer, ζ is the ζ-potential, and $\mu = 1.003 \times 10^{-3}$ Pa s is the viscosity of water at room temperature. Finally, to determine electrophoretic mobility, the electrophoretic velocity was divided by the electric field, E.

At the beginning of a measurement session, a test injection was performed in which the electrokinetically driven flow was stopped (by removing the applied electric field) and diffusion of the plug was monitored to check for hydrostatic pressure driven flow. Liquid levels in the four wells varied slightly with the shape of the well, and therefore, the volume of liquid in each well required to eliminate hydrostatic pressure gradients differed slightly, ranging from 54.7 to 56.3 μL. The volumes were noted and used in all subsequent measurements with a given set of wells. This procedure greatly enhanced the repeatability of our mobility measurements and allowed us to assume negligible pressure driven flow during current monitoring measurements.

Diffusivity was measured from the Gaussian broadening of a plug of analyte in a manner similar to that of Culbertson et al.[19] Briefly, a plug of analyte was electromigrated into the center of the field of view and all externally driven flow was stopped. The spatial distribution of the analyte fluorescence was recorded every 1 or 2 s using 50 or 100 ms exposures (Figure 4). The integrated intensity was constant over time, indicating negligible photobleaching. The intensity profiles fit well to a Gaussian, $I(t) = I_o \exp[(-x - x_o)^2/2\sigma^2]$, where I_o, x_o, and σ are the amplitude, position, and width of the intensity distribution, respectively. Diffusivity, D, was determined from a plot of $\sigma^2 = Dt$, versus time and did not depend on the time or frequency of exposure, confirming that the effects of photobleaching were negligible.

Downstream distances were determined from tick marks etched in the silica chip. For mobility measurements, images were recorded as far downstream as possible to minimize the systematic error that derives from uncertainty about the time of injection. In practice, this distance ranged from 2 to 10 mm, depending on the SNR. For diffusivity measurements, images were recorded ∼1.5 mm downstream to ensure narrow initial plugs while avoiding diffusive influx of analyte from the injection site.

The precision of our microfluidic diffusivity measurements, typically ± 2% (Table 2), is high compared to most in the literature, as first demonstrated by Culbertson et al.[19] Temperature control of the room in which measurements were made was the limiting factor.[34] In the time required to perform the five to 12 repeat measurements that were averaged to yield one data point, room temperature could vary by as much as 1 °C, causing the viscosity of water to change by ∼2%.

Thus, we made diffusivity measurements in the same microchannel setup and under the same conditions as our mobility measurements. The one exception was Ag_{13}:9C, which photobleached too rapidly. We therefore measured the diffusivity of Ag_{13}:9C (at pH 7.0) using fluorescence correlation spectroscopy (FCS) instead.

Diffusivity Measurements via Fluorescence Correlation Spectroscopy. We measured the diffusivity of Ag_{13}:9C (at pH 7.0) using fluorescence correlation spectroscopy (FCS). We checked for consistency with the microfluidic technique by measuring the diffusivity of Ag_{11}:9C (at pH 7.0) with FCS as well. Measurements were performed on solutions prepared with 25 μM DNA, 40 mM ammonium acetate (pH 7.0), 150 μM $AgNO_3$, 50 μM $NaBH_4$. Under these conditions, the red emitter Ag_{13}:9C forms within 1 h after reduction and is gradually oxidized, leading to the formation of the green emitter.[15] A 7-h-old, undiluted solution was used for FCS of the red emitter, Ag_{13}:9C. A 5-month-old, 10-fold diluted (in 40 mM ammonium acetate) solution was used for FCS of the green emitter, Ag_{11}:9C. The greater dilution factor compensated for the higher chemical yield of the green emitter.

The setup and procedure were as previously described,[35] with light sources and optics adapted to the spectra of these fluorophores. Both emitters were measured in an inverted, epi-illuminated geometry using a 60×, 1.2NA water immersion objective (UPLAN S APO, Olympus), specifically designed to image water-immersed objects up to 200 μm away from the coverslip. The objective was focused to a spot 25 μm above the coverslip to avoid complications arising from interactions between the fluorophores and the coverslip. A 50 μm diameter pinhole at the image plane of the microscope tube lens provided spatial filtering. To enable measurement times of many hours, an immersion oil with index of refraction n = 1.334 (Immersol W, Zeiss) was used instead of water, thereby avoiding evaporation and loss of optical coupling between the objective and coverslip. The coverslip formed the bottom of a 1 mL well (Nalge Nunc Interational, Lab-Tek 8 chamber). A sample volume of 500 μL was used to minimize the effects of evaporation.

Measurements of Ag_{13}:9C used the 543 nm line from a continuous wave HeNe laser (ThorLabs Model HGP005) with a 555 nm long-pass excitation dichroic (Semrock FF555-Di02) and a 60 nm band-pass filter centered at 620 nm (Chroma HQ620/60X) to filter the emission. Measurements of Ag_{11}:9C used the 400 nm line from a frequency-doubled mode-locked Ti:sapphire laser (fundamental pulse length, ∼100 fs; pulse repetition rate, 80 MHz; MaiTai Broadband, Spectra Physics) with a 405 nm long-pass excitation dichroic (Semrock R405-Di01) and a 488 nm long-pass edge filter (Semrock 488 RazorEdge).

Reference fluorophores, rhodamine B and Alexa Fluor 430 (Invitrogen A-10169), were used to determine the dimensions of the probe volume for 543 and 400 nm excitation, respectively, based on a 3D Gaussian model[36]

$$G(\tau) - 1 = \frac{1}{N}\left(1 + \frac{\tau}{\tau_d}\right)^{-1}\left(1 + \left(\frac{\omega}{z}\right)^2\left(\frac{\tau}{\tau_d}\right)\right)^{-1/2}$$

where $G(\tau) - 1$ is the fluorescence autocorrelation, τ is the lag time, N is the average number of fluorescent molecules in the probe volume, ω is the transverse radius of the probe volume, z is the half-length of the probe volume, and τ_d is the "crossing time" or the lag time at which the autocorrelation amplitude has decayed to approximately one-half of its maximum value, $G(0) - 1$. The probe volume radius is related to the crossing time and the translational diffusion coefficient (D) by

$$\omega = \sqrt{4D\tau_d}$$

Fits to the autocorrelation of ∼10 nM rhodamine B in water gave z/ω = 6.4 and τ_d = 59 μs. Given the known diffusivity of rhodamine B in water ($427 \pm 4\,\mu m^2/s$),[19] this crossing time implies a transverse radius of ω = 0.31 μm.

Fits to the autocorrelation of 100 nM Alexa Fluor 430 in 10 mM sodium phosphate, pH 6.9, gave a crossing time of τ_d = 44 μs and a probe volume aspect ratio of z/ω = 5.0. Estimating the diffusivity of Alexa Fluor 430 in water based on the known diffusivities of other Alexa Fluor dyes[37]

Table 1. Characterization of Fluorescein for in Situ ζ-Potential Calibration[a]

BGE	ζ-potential (mV): expt.	electrophoretic mobility [$\times 10^{-8}$ m^2/(V s)] expt.	electrophoretic mobility [$\times 10^{-8}$ m^2/(V s)] lit.[42]	charge state estimated (expt.)	charge state predicted (lit.)[41]
sodium acetate, pH 4.8	−86.7 ± 0.4	−1.17 ± 0.07	–	−0.70 ± 0.04	−0.76
sodium phosphate, pH 7.0	−94.4 ± 0.3	−2.92 ± 0.06	–	−1.75 ± 0.06	−1.79
sodium borate, pH 9.2	−114 ± 0.3	−3.20 ± 0.08	−3.3 ± 0.1 (pH 8.5)	−1.92 ± 0.06	−1.998

[a] All experiments were performed in a silane-coated 20 μm deep borosilicate channel. ζ-Potentials were obtained by current monitoring at three different electric field strengths and repeated six times each. CM was immediately followed by electrokinetic injections. Injections were run with two different electric fields and repeated six times each. Charge state was estimated using the Nernst−Einstein equation with a diffusion coefficient, $D = 4.25 \times 10^{-10}$ m^2/s, from the most precise measurement available to date[19] and predicted using pK_a values of 4.31 and 6.43 for the two ionizable groups of fluorescein.[41] Quoted errors are one standard deviation.

Table 2. Measured Elctrophoretic Mobilities, Diffusivities, and Corresponding Effective Hydrodynamic Radii at pH 7.0[a]

species	electrophoretic mobility [$\times 10^{-8}$ m^2/(V s)]	diffusivity (μm^2/s)	hydrodynamic radius (nm)
Ag_{11}:9C	−4.31 ± 0.03	155 ± 3	1.39 ± 0.03
Ag_{13}:9C	−4.34 ± 0.06	120 ± 5	1.80 ± 0.08
FAM:9C	−4.55 ± 0.05	137 ± 2	1.58 ± 0.02
FAM:9C5A	−4.24 ± 0.05	116 ± 2	1.86 ± 0.02
Ag_{11}:9C5A	−4.25 ± 0.02	156 ± 2	1.38 ± 0.02
Ag_n:12C	−4.76 ± 0.06	133 ± 3	1.62 ± 0.04

[a] Electrophoretic mobility measurements were performed at two different electric fields and were repeated at least nine and up to 46 times for each species. With the exception of Ag_{13}:9C, which was measured by FCS, diffusivity measurements were repeated at least five and up to 12 times. *R*-Values of the linear regression of σ^2/t were ≥0.9998 in all cases. Hydrodynamic radii were calculated using the Stokes−Einstein relation, assuming spherical particles at $T = 296$ K (room temperature). Errors are one standard deviation.

(409 ± 11 μm^2/s), this crossing time implies a transverse radius of $\omega = 0.27$ μm.

FCS data for the Ag:DNA emitters are provided in the Supporting Information. Again, fits to the autocorrelation functions provided a measure of the crossing times from which we calculated their respective diffusion coefficients, according to

$$D_{\text{Ag:DNA}} = D_{\text{reference}} \frac{\tau_{\text{d, reference}}}{\tau_{\text{d, Ag:DNA}}}$$

Autocorrelation functions of Ag_{11}:9C were fit using the 3D Gaussian model above, with the probe volume aspect ratio fixed to the value determined from the Alexa Fluor 430 measurements. The fits gave crossing-times that decreased with increasing pump powers, indicative of photobleaching. To minimize the influence of photobleaching on the crossing times, we used the lowest pump powers giving sufficient count rates to measure the autocorrelation function on the time scale of a few hours. At low pump powers of 2.0, 4.6, 6.8, and 8.6 μW, the Ag_{11}:9C crossing time decreased linearly with increasing pump power. Extrapolation of this linear fit to zero pump power gave an upper bound on the crossing time of 124 μs, and the crossing time from the 2.0 μW autocorrelation function gave a lower bound of 114 μs. The corresponding bounds on the Ag_{11}:9C diffusivity were 147 and 160 μm^2/s, consistent with the diffusivity measured by the microfluidic technique (Table 2).

The autocorrelation function of Ag_{13}:9C showed clear blinking signatures, even at low pump powers. Fixing the probe volume aspect ratio to the value determined from the rhodamine B measurements, the data was fit with the modified model[38,39]

$$G(\tau) - 1 = \frac{1}{N}\left(1 + \frac{d}{1-d}e^{-\tau/\tau_{\text{blink}}}\right)\left(1 + \frac{\tau}{\tau_d}\right)^{-1}\left(1 + \left(\frac{\omega}{z}\right)^2\left(\frac{\tau}{\tau_d}\right)\right)^{-1/2}$$

where τ_{blink} is the dark-state lifetime, and d is the fraction of emitters in the dark state.

The Ag_{13}:9C autocorrelation function was measured at 110 nW, a considerably lower pump power than used for any of the Ag_{11}:9C. This was possible because differences in nanocluster brightness resulted in collection of about 6 times more photons per second per Ag_{13}:9C than per Ag_{11}:9C at this low excitation intensity. The fit gave a dark-state lifetime of 20 μs, similar to those previously reported for other Ag:DNAs,[8] and a crossing time of 210 μs. Crossing times at a pump power of 1 μW agreed with this value to within 3%. The corresponding Ag_{13}:9C diffusivity is 120 ± 5 μm^2/s.

Fluorometry. Solution fluorescence was measured with a Cary Eclipse fluorometer (Varian). Peak excitation and emission wavelengths were determined from 2D Gaussian fits to the raw data.[14]

Molecular Graphics. Coordinate files for the molecular graphics of possible Ag_{11}:9C and Ag_{13}:9C structures displayed in Figure 7 were generated using the TINKER implementation of AMBER99, converted using OpenBabel, and visualized using Schrodinger's Maestro visualization package.

To model silver, a new atom was appended to the AMBER99 force field. This atom was of TINKER class sulfur, with some modifications. Namely, its van der Waals radius was adjusted to match the experimental van der Waals radius of atomic silver and it was given no charge. Cluster configurations were obtained from ground state, time-dependent density functional theory (TDDFT) calculations (in vacuum) made by Soto-Verdugo as described elsewhere.[40] The clusters were constrained to adopt the calculated ground state structure using the "restrain-position" modifier in TINKER's ".key" file.

DNA−silver interactions were modeled by imposing geometrical constraints. Specifically, interactions were modeled using the "restrain-distance" modifier to mimic bonds between select cytosine N(3)−Ag atom pairs in the ".key" file. Bond distance was based on TDDFT calculations of cytidine−Ag bonds (in vacuum).[40] The strength of the restraint was larger for cytosine N(3)−Ag pairs involving Ag atoms with greater exposure on the cluster surface. A total of seven and eight such pairwise interactions were imposed for Ag_{11}:9C and Ag_{13}:9C, respectively.

Coordinate files were computed using TINKER's "minimize" function. The GBSA solvent model for water was used throughout calculations. The "restrain-position" modifier was used selectively to encourage assumed conformations, as well as overcome computational difficulties. For example, to encourage a hairpin fold in the Ag_{13}:9C structure, the DNA ends were initially held close together. The rms cutoff was

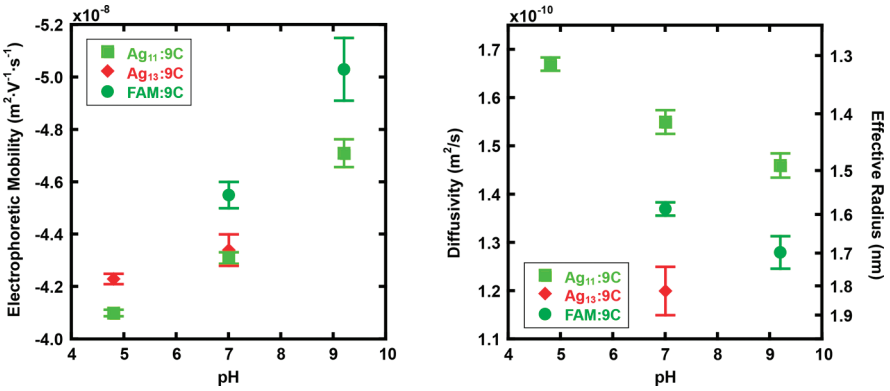

Figure 5. Measured electrophoretic mobilities (left), diffusivities, and corresponding effective hydrodynamic radii (right) for the two 9C-based Ag:DNAs (Ag_{11}:9C and Ag_{13}:9C) and for the 9C sequence without Ag (FAM:9C). All three were characterized in phosphate buffer (pH 7.0). Ag_{13}:9C was not observable in borate buffer (pH 9.2) and its diffusivity was measured only at pH 7.0.

incrementally decreased to a final value of 0.01 kcal/mol to ensure complete local minimization.

Thus, this modeling exercise assures the feasibility of a structure (e.g., with respect to bond lengths, bond angles, and excluded volume of the DNA oligomer) but not its plausibility.

RESULTS

In Situ ζ-Potential Calibration. The ζ-potential of a channel-electrolyte system determines the electroosmotic velocity for a given electric field and is thus a crucial parameter for quantitative capillary electrophoresis-based measurements. However, as discussed in the methods section, sensitivity to changes in buffer composition and surface chemistry, which inevitably occur with use, make it difficult to rely on or even make comparison with ζ-potentials reported in the literature.[31] We addressed this issue by measuring the ζ-potential in pristine silanized channels immediately prior to performing electrokinetic injections on the organic dye fluorescein. The resulting measurements of the electrophoretic mobility of fluorescein compared well with published values and corresponded to the expected charge states at three different pH conditions, based on known pK_a's of fluorescein's two titratable groups (Table 1). This good agreement gave us confidence to use fluorescein's electrophoretic mobility as an in situ measurement of the ζ-potential of our channels during subsequent injection experiments.

Using an in situ standard greatly improved the accuracy and repeatability of our electrophoretic mobility measurements. We report the electrophoretic mobility of fluorescent Ag:DNA nanoclusters with an accuracy of ±3.5%, limited by uncertainty in the imposed electric field, and a precision $\leq \pm 10^{-9}$, as given by the standard deviation of the samples (Table 2). This represents a significant improvement over data in the literature, which have error bars spanning ±12%[19,31,43] and precision no better than $\pm 10^{-8}$.

Electrophoretic Mobility and Diffusivity. We measured the electrophoretic mobility and diffusivity in phosphate buffer (pH 7.0) of four Ag:DNA fluorophores made from three similar DNA sequences (Figure 1): a hairpin with nine cytosines in the loop (9C), the same hairpin with a single base change to destabilize the stem (9C5A), and the same hairpin with a three base addition to enlarge the loop (12C). For insight into the effect of silver binding per se, we made the same measurements on DNA sequences 9C and 9C5A without silver. These were rendered fluorescent by the covalent attachment of a fluorescein label (FAM) and are therefore referred to as FAM:9C and FAM:9C5A, respectively. We made most of the diffusivity measurements in the same microchannel setup and under the same conditions as the electrophoretic mobility measurements, using the static technique of Culbertson et al.[19] The only exception was Ag_{13}:9C, which photobleached too quickly and for which diffusivity was measured by FCS.[44] The results are compiled in Table 2.

The 9C sequence was chosen because it supports two Ag:DNA fluorophores with distinct spectral characteristics and different numbers of silver atoms.[15] One is a red emitter (λ_{ex} = 565 nm, λ_{em} = 620 nm) that has 13 silver atoms, herein referred to as Ag_{13}:9C. The other is a green emitter (λ_{ex} = 405 nm, λ_{em} = 525 nm) that has 11 silver atoms, herein referred to as Ag_{11}:9C. Mass spectra of the Ag:DNA species used here are without peaks corresponding to species with smaller numbers of silver atoms,[45] indicating that the silver atoms in these fluorophores are binding as a single cluster. We sought to determine whether silver atom number is the primary difference between these fluorophores or whether they also differ significantly in structure and charge state.

We found that the two Ag:9C emitters differ perceptibly in electrophoretic mobility. The difference in electrophoretic mobility (<1%) at pH 7.0 was smaller than the systematic error but could be clearly resolved when both species were present in the same solution[15] and measurements were made in rapid succession (Figure S-5, Supporting Information). In an effort to improve resolution, we repeated these measurements at non-neutral pH.

Fluorescence spectra were the same in the three buffers we used (Figure S-3, Supporting Information), but diffusivity and electrophoretic mobility changed (Figure 5). At pH 4.8 (acetate buffer), the electrophoretic mobilities of both Ag:9C species became less negative, consistent with the absolute reduction of their negative charge expected at lower pH. Interestingly, the effect was less pronounced for Ag_{13}:9C than for Ag_{11}:9C, enhancing the difference in electrophoretic mobilities to an easily resolvable ~3%. We measured the diffusivity of only Ag_{11}:9C at this low pH and found that it increased, indicating that, at pH 7.0, this Ag:DNA complex is not restricted to its most compact state.

At pH 9.2 (borate buffer), the trend continued. Electrophoretic mobility became more negative and diffusivity decreased. We refer to results for Ag_{11}:9C alone because Ag_{13}:9C was unobservable at this pH. Again, higher pH corresponded to a more negatively charged Ag:DNA complex and a less compact conformation. We

dx.doi.org/10.1021/la200837z |*Langmuir* 2011, 27, 8923–8933

note, however, that the effect on electrophoretic mobility was remarkably large: Ag_{11}:9C moved ~10% faster at pH 9.2 than at pH 7.0. We found a similar ~10% enhancement in electrophoretic mobility for FAM:9C using the same buffers, indicating that the unusually large effect is not specific to Ag:DNA but may be particular to borate buffer. Along these lines, Stellwagen et al. have reported a tendency for borate to form a complex with DNA, thereby increasing its negative charge beyond what would be expected on the basis of counterion condensation alone[46] (see discussion below).

The differential pH dependence of electrophoretic mobility of Ag_{13}:9C and Ag_{11}:9C is the first indication that the red and green emitters differ significantly in structure. The diminished effect of pH on electrophoretic mobility of Ag_{13}:9C suggests that it is less able to compactify than Ag_{11}:9C. The absence of Ag_{13}:9C fluorescence altogether at high pH suggests that the emissive core is destroyed as the complex swells to accommodate additional negative charge. Taken together, these observations lead us to advance the hypothesis that the red emitter is more rigidly constructed than the green one. In what follows, we refine and develop this hypothesis based on measurements made at neutral pH.

FAM:9C, with its known hairpin structure comprised of a rigid stem and a flexible loop, serves as our first reference point. It exhibited significantly more negative electrophoretic mobility (~5−7%) than either Ag:9C, but not as much more as expected (~8%)[47] given the negative charge of the FAM moiety (Table 1). Since the two main factors determining electrophoretic mobility are charge and size, the observation that the added charge of FAM does not fully account for the relative electrophoretic mobility of FAM:9C suggests that silver binding induces important structural changes in the 9C DNA sequence. This is consistent with the known tendency for silver to bind directly to adenosine and cytosine bases.[22]

Silver-binding-induced structural changes are also consistent with our independent diffusivity measurements. Diffusivity of Ag_{11}:9C is ~13% larger than that of FAM:9C, which is, in turn, ~14% larger than that of Ag_{13}:9C. The nearly 30% difference in diffusivities of the Ag_{11}:9C and Ag_{13}:9C emitters leads us to conclude that Ag_{11}:9C is a compact structure, while Ag_{13}:9C is not.

Recall that Ag_{13}:9C and Ag_{11}:9C have nearly identical electrophoretic mobilities at neutral pH. Given their nearly identical composition, how might Ag_{13}:9C present enough additional negative charge relative to Ag_{11}:9C to offset its 30% lower diffusivity? One possibility is that the structure of Ag_{13}:9C is an extended one. If, for example, the phosphate backbone of both the stem and loop regions were roughly coplanar, in a lollipop- or cigar-like conformation, the structure could sustain more charge and/or could become oriented under electroosmotic flow so as to present less hydrodynamic resistance than when freely diffusing.

This insight into the structure of Ag_{13}:9C is reinforced by a comparison with FAM:9C5A. Recall that FAM:9C5A is identical to FAM:9C save for a mismatch in the fifth base pair from the bottom of the loop. This mutation reduced both the electrophoretic mobility (~7%) and the diffusivity (~18%) of FAM:9C5A relative to FAM:9C, indicating that the mismatched base pair successfully destabilized the hairpin. Interestingly, despite the negative charge added by FAM, electrophoretic mobility of FAM:9C5A was also significantly slower (~10%) than that of Ag_{13}:9C, while their diffusivities were comparable (<3%). Therefore, although less compact than FAM:9C, Ag_{13}:9C is not as swollen a structure as FAM:9C5A. Again the possibility that

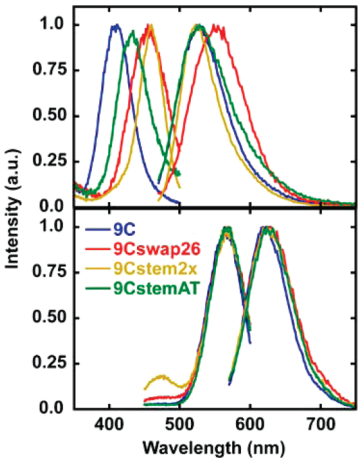

Figure 6. Fluorescence excitation and emission spectra of green (top) and red (bottom) Ag:DNA fluorophores made from the 9C DNA sequence and three variants with different base pairs in the hairpin stem (described in the text). Excitation spectra were based on fluorescence collected at the emission maximum. Emission spectra were collected while illuminating at the excitation maximum for each fluorophore. See Figure S-2 (Supporting Information) for more detailed contour plots.

Ag_{13}:9C is an extended structure provides a reasonable explanation.

Thoughtful mutation of the 9C sequence in an Ag:DNA context provides another path to structural information. A comparison of the fluorescence spectra of Ag:DNAs formed from sequences that maintain the native hairpin structure of the 9C sequence is particularly illuminating. We focus on three such variants that, like 9C, each support two Ag:DNA fluorophores, one red and one green. The most subtle variant is identical to the 9C, except that the second and sixth base pairs in the stem are swapped (9Cstem26). The next variant has the same loop and stem sequence plus another seven base pairs (9Cstem2×), raising the predicted melting temperature of the hairpin structure[48] from 48 to 60 °C. In the most dramatic variant (9CstemAT), every cytosine in the stem has been changed to a thymine and the corresponding guanine to an adenine, reducing the predicted melting temperature[48] to 26 °C. Despite all their differences, the red Ag:DNA formed by these sequences have nearly identical fluorescence spectra. The green Ag:DNA, on the other hand, vary in both excitation and emission maxima (Figure 6). We conclude that the emissive core of red Ag_{13}:9C resides primarily in the hairpin loop, whereas the emissive core of green Ag_{11}:9C involves bases outside the loop.

Further support for this conclusion comes from the 9C5A sequence, for which our electrophoretic mobility and diffusivity measurements indicate the hairpin structure is disrupted (discussed above). This sequence does not support a red emitter under our synthesis conditions. It forms Ag_{11}:9C5A, a green emitter identical to Ag_{11}:9C both spectrally (Figure S-2, Supporting Information) and in the number of silver atoms bound.[49] The electrophoretic mobility of Ag_{11}:9C5A was within 1.5% of that of Ag_{11}:9C, and their diffusivities were indistinguishable (Table 2). Taken all together, these observations indicate that these two green emitters have the same highly compact structure and raise the possibility that this structure is not hairpin-like.

To gain similar structural insight into the red emitter, we used 12C, a DNA sequence identical to 9C except that it has three

extra cytosines in the hairpin loop. When reduced in the presence of silver, 12C forms Ag_n:12C, a red emitter with an excitation spectrum identical to and an emission spectrum only a few nanometers red-shifted from those of Ag_{13}:9C (Figure S-2, Supporting Information).

The electrophoretic mobility of Ag_n:12C was nearly 10% more negative and its diffusivity was 11% *greater* than that of Ag_{13}:9C (Table 2). It therefore appears that, while Ag_{13}:9C is extended, Ag_n:12C is compact. If we take the spectral similarity as an indication that Ag_n:12C has $n = 13$, we might expect the silver cluster in these red emitters to be bound exclusively to bases in the loop. If so, the greater compactness of Ag_{13}:12C might be attributed to the larger loop maintaining flexibility where the loop meets the stem.

DISCUSSION

Structure. From measurements of electrophoretic mobility and diffusivity on a select set of Ag:DNA emitters, we have determined that the two spectrally distinct emitters stabilized by the 9C sequence, the green emitting Ag_{11}:9C and the red emitting Ag_{13}:9C, differ in structure as well as Ag-atom number. The green emitter is compact, even more so than the hairpin its DNA adopts in the absence of silver. The red emitter is extended, diffusing more slowly than a disrupted hairpin but migrating more quickly when subject to an electric field.

A comparison of fluorescence spectra from Ag:DNAs on related sequences suggests that the red emitter requires a hairpin conformation but keeps its emissive core out of contact with bases in the double-stranded stem, whereas the green emitter has a core that interacts with bases in the stem, possibly even disrupting the hairpin structure altogether.

The two structural extremes consistent with our findings are illustrated in Figure 7. To generate these illustrations, we used molecular modeling software to manipulate a virtual "ball-and-stick" mechanical model (see the methods). The resulting structures respect known bond lengths and angles and avoid steric conflicts, but are not necessarily energetically or kinetically allowed. In other words, they are possible structures, but not necessarily plausible ones save for the fact that they capture the qualitative features deduced above.

Effective Charge. Having independent measurements of both electrophoretic mobility and diffusivity at our disposal, it is natural to consider their ratio as an indicator of the charge on the various species we studied. An effective charge Z can be computed from the Nernst−Einstein equation

$$Z = \frac{RT}{F}\frac{\mu_{ep}}{D}$$

where μ_{ep} is the electrophoretic mobility, D is the diffusivity, and R, T, and F are the gas constant, the temperature, and the Faraday constant, respectively. It is important to note, however, that this relation assumes small, roughly spherical ions—a condition that often fails to describe DNA. Nkodo et al.[50] have reported failure of the Nernst−Einstein relation when applied to DNA molecules with ≥400 bp. More recently, Stellwagen et al.[51] have shown that the ratio μ_{ep}/ZD is not constant for single-stranded or double-stranded DNA as small as 10 repeat units (bases or base pairs) with significant secondary structure. We therefore report the effective charge of our analytes, as calculated using the Nernst−Einstein relation, graphically versus their effective hydrodynamic radii, as calculated using the Stokes−Einstein relation (Figure 8) and seek qualitative rather than strictly quantitative insights.

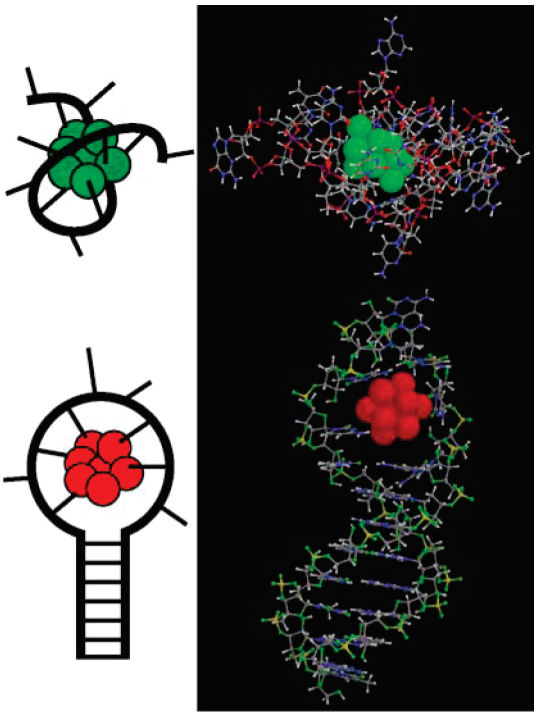

Figure 7. Schematic and steric illustrations of extremely compact Ag_{11}:9C (top) and extended Ag_{13}:9C (bottom) conformations suggested by the results. Steric illustrations are virtual mechanical ball-and-stick mechanical models generated using the TINKER implementation of AMBER99, converted using OpenBabel, and drawn using Schrodinger's Maestro visualization package (see methods section for details). As such, the structures depicted are sterically feasible but not necessarily energetically or kinetically plausible.

The most striking trend in the data thus plotted is the linear relationship between charge and size exhibited by Ag_{11}:9C at different pH (Figure 8, solid line) which extrapolates to fit data for FAM:9C reasonably well (Figure 8, dashed line). It is well established that the concentration of negative phosphates in DNA can be high enough to condense counterions,[52] a phenomenon known in colloid physics as charge renormalization.[53] A linear relationship between effective charge and polyion size is consistent with counterion condensation on spherical polyelectrolytes,[54] implying that the compact species Ag_{11}:9C, FAM:9C and even Ag_n:12C have aspect ratios close to 1. The two species not captured by this linear relationship are those with the largest effective radius, Ag_{13}:9C and FAM:9C5A, reinforcing the notion that their conformation is an extended one.

Counterion condensation also explains (i) the low effective negative charge of our analytes relative to the number of ionizable phosphodiester bonds ($pK_a \sim 1$)[55] in their DNA sequences[56] and (ii) the linear increase in effective negative charge upon increasing pH observed for both Ag_{11}:9C and FAM:9C (Figure 9). The observation that varying pH causes not only the charge but also the size of Ag_{11}:9C to increase suggests an explanation for the absence of fluorescent Ag_{13}:9C at basic pH: perhaps, as the already extended structure swells to accommodate additional negative charge, it breaks one or more silver−DNA bonds, destroying the emissive electronic state.

While our data clearly suggest that Ag_{13}:9C has an extended conformation, it is also possible that the silver cluster in the Ag_{11}:9C species is more positively charged than in the red emitter,

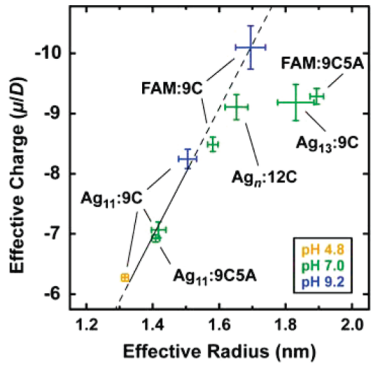

Figure 8. Effective charge as a function of effective hydrodynamic radius. Effective charge was calculated via Nernst−Einstein based on our independent measurements of electrophoretic mobilities and diffusivities for all analytes. The linear correlation is consistent with counterion condensation for roughly spherical structures. The two largest species, Ag_{13}:9C and FAM:9C5A, have a different effective charge/size ratio, reinforcing the notion that they are extended rather than compact structures.

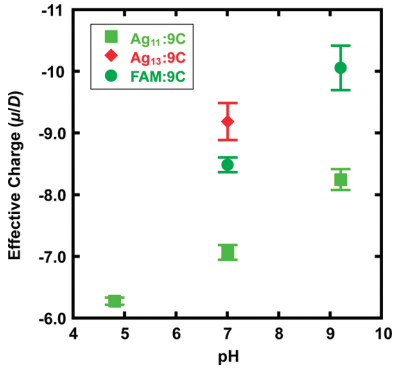

Figure 9. Effective charge as calculated via Nernst−Einstein based on the measured electrophoretic mobilities and diffusivities for Ag_{11}:9C and FAM:9C at different pH and for Ag_{13}:9C at pH 7.0 only.

enhancing the difference in electrophoretic mobility. It is known that the Ag_{11}:9C and Ag_{13}:9C emitters are linked by an oxidation reaction, with Ag_{11}:9C being more positively charged.[15,57] Further, other studies provide precedent for positively charged silver nanoclusters.[17,58,59] Our results at pH 7.0 are consistent with the green emissive core being two units more positively charged than the red, but it must be noted that applying Nernst−Einstein to an extended structure results in an overestimate of its charge, so it is possible that two emitters differ by only one unit of charge or not at all.

SUMMARY AND CONCLUDING REMARKS

We report the electrophoretic mobility and diffusivity measurements of fluorescent Ag:DNA nanoclusters in fused-silica micrometer-scale channels and demonstrate their utility for deciphering aspects of Ag:DNA structure.

The in situ calibration of a reference analyte allowed us to measure electrophoretic mobility with unprecedented accuracy (±3.5%) and precision ($\leq \pm 10^{-9}$ m^2 V^{-1} s^{-1}). The static technique of Culbertson et al.[19] allowed us to measure diffusivity with similarly high precision in the very same environment in which mobility measurements were performed for all but the most photolabile species. Taken together, electrophoretic mobility and diffusivity measurements provided a characterization of both the effective size and the effective charge of the Ag:DNA.

We focused on two Ag:DNA emitters that are stabilized by the same DNA sequence (9C). By comparing the two to each other, to Ag:DNA species of related sequence and spectrum, and to a subset of Ag-free DNA oligomers, we found that the binding of Ag induces significant structural changes. In the case of the well-characterized green emitter Ag_{11}:9C, we found that the Ag:DNA adopts a compact structure, possibly disrupting the hairpin motif native to its DNA oligomer (Figure 7, top). By contrast, the red emitter that forms on the same DNA oligomer, Ag_{13}:9C, appears to be an extended structure, possibly stiffening the native oligomer's hairpin conformation (Figure 7, bottom).

Further structural insight came from fluorometry measurements on Ag:DNAs made from the 9C sequence and three variants with different base pairs in the hairpin stem (Figure 6). Consistent with the conformations proposed above, we found that the emissive core of red Ag_{13}:9C resides primarily in the hairpin loop, whereas the emissive core of green Ag_{11}:9C involves bases outside the loop.

The small but measurable differences in electrophoretic mobility we measured for the spectrally distinct Ag_{11}:9C and Ag_{13}:9C may recommend them for use in microfluidic-based bioanalytical devices. For example, Khurana and Santiago use fluorescent mobility markers based on organic dyes to achieve separation and indirect detection of nonfluorescent species.[60] Their technique leverages isotachophoresis (ITP) for both concentration and separation of analytes. It relies on fluorescent markers that differ in electrophoretic mobility. The smaller the difference in mobility of distinguishable markers, the greater the potential resolution in mobility of nonfluorescent analytes captured between the markers. Our results suggest that fluorescent Ag:DNA nanoclusters may provide a library of fluorescent markers that would improve the dynamic range and resolution of the ITP-based assay.

ASSOCIATED CONTENT

Supporting Information. Effect of storage conditions; fluorescence spectra; FCS data; electrophoretic discrimination of Ag_{11}:9C and Ag_{13}:9C at pH 7.0. This material is available free of charge via the Internet at http://pubs.acs.org/.

AUTHOR INFORMATION

Corresponding Author

*E-mail: deborah@physics.ucsb.edu.

Present Addresses

[⊥]Drittes Physikalisches Institut, Georg-August-University, Göttingen, Germany.

ACKNOWLEDGMENT

We are grateful to Eugene Petrov for discussions of FCS and exploratory measurements, to Fyl Pincus for discussions of charge renormalization, and to Tommy Foley for molecular graphic renditions of possible Ag:DNA nanocluster structures. This research was supported in part by the National Science Foundation (Grant CHE-0848375) and in part by the Army Research Office (Contract W911NF-09-D-0001) through the Institute for Collaborative Biotechnologies at UCSB. This work

was performed, in part, at the Center for Integrated Nanotechnologies, a U.S. Department of Energy, Office of Basic Energy Sciences user facility at Los Alamos National Laboratory (Contract DE-AC52-06NA25396) and Sandia National Laboratories (Contract DE-AC04-94AL85000).

REFERENCES

(1) (a) Diaspro, A., Ed. *Confocal and Two-Photon Microscopy: Foundations, Applications and Advances*; Wiley-Liss: New York, 2002; (b) Klar, T. A.; Hell, S. W. *Optics Lett.* **1999**, *24*, 954–956. (c) Bates, M.; Huang, B.; Dempsey, G. T.; Zhuang, X. *Science* **2007**, *317*, 1749–1753. (d) Shao, L.; Isaac, B.; Uzawa, S.; Agard, D. A.; Sedat, J. W.; Gustafsson, M. G. L. *Biophys. J.* **2008**, *94*, 4971–4983.

(2) (a) Checovich, W. J.; Bolger, R. E.; Burke, T. *Nature* **1995**, *375*, 254–256. (b) Chiang, P. W.; Song, W. J.; Wu, K. Y.; Korenberg, J. R.; Fogel, E. J.; Van Keuren, M. L.; Lashkari, D.; Kurnit, D. M. *Genome Res.* **1996**, *6*, 1013–1026. (c) Selvin, P. R. *Nat. Struct. Biol.* **2000**, *7*, 730–734. (d) Hess, S. T.; Huang, S.; Heikal, A. A.; Webb, W. W. *Biochemistry* **2002**, *41*, 697–705.

(3) (a) Herzenberg, L. A.; Parks, D.; Sahaf, B.; Perez, O.; Roederer, M.; Herzenberg, L. A. *Clin. Chem.* **2002**, *48*, 1819–1827. (b) Squires, T. M.; Quake, S. R. *Rev. Mod. Phys.* **2005**, *77*, 977–1026. (c) Whitesides, G. M. *Nature* **2006**, *442*, 368–373.

(4) Fei, X.; Gu, Y. *Prog. Nat. Sci.* **2009**, *19*, 1–7.

(5) Miyawaki, A.; Sawano, A.; Kogure, T. *Nat. Cell Biol.* **2003**, *5*, S1–S7.

(6) Jaiswal, J. K.; Simon, S. M. *Trends Cell Biol.* **2004**, *14*, 497–504.

(7) (a) Zheng, J. Fluorescent Noble Metal Nanoclusters. Dissertation, Georgia Institute of Technology, 2005. (b) Xu, H.; Suslick, K. S. *Adv. Mater.* **2010**, *22*, 1078–1082.

(8) Vosch, T.; Antoku, Y.; Hsiang, J.-C.; Richards, C. I.; Gonzalez, J. I.; Dickson, R. M. *Proc. Natl. Acad. Sci. U. S. A.* **2007**, *104*, 12616–12621.

(9) Richards, C. I.; Choi, S.; Hsiang, J.-C.; Antoku, Y.; Vosch, T.; Bongiorno, A.; Tzeng, Y.-L.; Dickson, R. M. *J. Am. Chem. Soc.* **2008**, *130*, 5038–5039.

(10) Petty, Jeffrey, T.; Zheng, J.; Hud, N. V.; Dickson, R. M. *J. Am. Chem. Soc.* **2004**, *126*, 5207–5212.

(11) (a) Yu, J.; Choi, S.; Richards, C. I.; Antoku, Y.; Dickson, R. M. *Photochem. Photobiol.* **2008**, *84*, 1435–1439. (b) Yu, J.; Choi, S.; Dickson, R. M. *Angew. Chem. Int. Ed.* **2009**, *48*, 318–320.

(12) (a) Guo, W.; Yuan, J.; Wang, E. *Chem. Commun.* **2009**, 3395–3397. (b) Lan, G.-Y.; Huang, C.-C.; Chang, H.-T. *Chem. Commun.* **2010**, *46*, 1257–1259.

(13) Richards, C. I.; Hsiang, J.-C.; Senapati, D.; Patel, S.; Yu, J.; Vosch, T.; Dickson, R. M. *J. Am. Chem. Soc.* **2009**, *131*, 4619–4621.

(14) Gwinn, E.; O'Neill, P.; Guerrero, A. J.; Bouwmeester, D.; Fygenson, D. *Adv. Mater.* **2008**, *20*, 279–283.

(15) O'Neill, P. R.; Velazquez, L. R.; Dunn, D. G.; Gwinn, E. G.; Fygenson, D. K. *J. Phys. Chem. C* **2009**, *113*, 4229–4233.

(16) Sharma, J.; Yeh, H.-C.; Yoo, H.; Werner, J. H.; Martinez, J. S. *Chem. Commun.* **2010**, *46*, 3280–3282.

(17) Sengupta, B.; Springer, K.; Buckman, J. G.; Story, S. P.; Abe, O. H.; Hasan, Z. W.; Prudowsky, Z. D.; Rudisill, S. E.; Degtyareva, N. N.; Petty, J. T. *J. Phys. Chem. C* **2009**, *113*, 19518–19524.

(18) Napoli, M.; Eijkel, J. C. T.; Pennathur, S. *Lab Chip* **2010**, *10*, 957–985.

(19) Culbertson, C. T.; Jacobson, S. C.; Michael Ramsey, J. *Talanta* **2002**, *56*, 365–373.

(20) Krichevsky, O.; Bonnet, G. *Rep. Prog. Phys.* **2002**, *65*, 251–297.

(21) Markham, N. R.; Zuker, M. *Nucleic Acids Res.* **2005**, 33, W577–W581.

(22) Ono, A.; Cao, S.; Togashi, H.; Tashiro, M.; Fujimoto, T.; Machinami, T.; Oda, S.; Miyake, Y.; Okamoto, I.; Tanaka, Y. *Chem. Commun* **2008**, 4825–4827.

(23) Megger, D. A.; Muller, J. *Nucleosides, Nucleotides Nucleic Acids* **2010**, *29*, 27–38.

(24) Andersen, M. B.; Bruus, H.; Bardhan, J. P.; Pennathur, S. *J. Colloid Interface Sci.* 2011, to appear.

(25) White, R. J.; Ervin, E. N.; Yang, T.; Chen, X.; Daniel, S.; Cremer, P. S.; White, H. S. *J. Am. Chem. Soc.* **2007**, *129*, 11766–11775.

(26) Bharadwaj, R.; Santiago, J. G. *J. Fluid Mech.* **2005**, *543*, 57–92.

(27) Channels that were stored in water showed intense wall adsorption effects (documented in Supporting Information), suggesting that their silane coatings had degraded.

(28) Rasband, W. S. *ImageJ*; 2009;http://rsb.info.nih.gov/ij/.

(29) Sze, A.; Erickson, D.; Ren, L.; Li, D. *J. Colloid Interface Sci.* **2003**, *261*, 402–410.

(30) Hunter, R. J. *Zeta Potential in Colloid Sciences*; Academic Press: New York, 1981.

(31) Bazant, M. Z.; Kilic, M. S.; Storey, B. D.; Ajdari, A. *Adv. Colloid Interface Sci.* **2009**, *152*, 48–88.

(32) Pennathur, S.; Santiago, J. G. *Anal. Chem.* **2005**, *77*, 6772–6781.

(33) Bharadwaj, R.; Santiago, J. G.; Mohammadi, B. *Electrophoresis* **2002**, *23*, 2729–2744.

(34) Illumination intensity, electric field strengths, and duration were all so low as to make infrared and Joule heating negligible.

(35) Sengupta, B.; Ritchie, C. M.; Buckman, J. G.; Johnsen, K. R.; Goodwin, P. M.; Petty, J. T. *J. Phys. Chem. C* **2008**, *112*, 18776–18782.

(36) Rigler, R.; Kask, P. *Eur. Biophys. J.* **1993**, *22*, 169–175.

(37) The molecular weights of Alexa Fluors 350, 488, and 594 are 410, 643, and 820 g/mol, respectively.[61] Their diffusivities in bulk water are 570, 430, and 370 $\mu m^2/s$, respectively.[62] The diffusivity of Alexa Fluor 430 (702 g/mol) was estimated from the least-squared error fit to $D = a + bMW^{-1/3}$ for the other three Alexa Fluors.

(38) Widengren, J.; Rigler, R.; Mets, U. *J. Fluoresc.* **1994**, *4*, 255–258.

(39) Petrov, E. P.; Schwille, P. In *Standardization and Quality Assurance in Fluorescence Measurements II: Bioanalytical and Biomedical Applications*; Resch-Genger, U., Ed.; Springer: New York, 2008; Vol. 6; pp 145−197.

(40) Soto-Verdugo, V.; Metiu, H.; Gwinn, E. E. *J. Chem. Phys.* **2010**, *132*, 195102–195110.

(41) Sjöback, R.; Nygren, J.; Kubista, M. *Spectrochim. Acta Part A* **1995**, *51*, L7–L21.

(42) Harrison, D. J.; Manz, A.; Fan, Z.; Luedi, H.; Widmers, M. *Anal. Chem.* **1992**, *64*, 1926–1932.

(43) Mosier, B. P.; Molho, J. I.; Santiago, J. G. *Exp. Fluids* **2002**, *33*, 545–554.

(44) Consistency between microfluidic and FCS diffusivity measurements was demonstrated for Ag_{11}:9C, as discussed in the methods section.

(45) P. O'Neill et al. , in preparation.

(46) Stellwagen, N. C.; Gelfi, C.; Righetti, P. G. *Biopolymers* **1997**, *42*, 687–703.

(47) Assuming charge-renormalization due to counterion condensation affects the negative charges on FAM and DNA similarly. At pH 7.0, we expect (FAM + DNA)/(DNA) = 24.75/23 = 1.076. At pH 9.2, we expect (FAM + DNA)/(DNA) = 24.92/23 = 1.083.

(48) Zuker, M. *Nucleic Acids Res.* **2003**, *31*, 3406–3415.

(49) The number of silver atoms in Ag_{11}:9C5A was determined by mass spectroscopy in a manner similar to that described by O'Neill et al.[15]

(50) Nkodo, A. E.; Garnier, J. M.; Tinland, B.; Ren, H.; Desruisseaux, C.; Mccormick, L. C.; Drouin, G.; Slater, G. W. *Electrophoresis* **2001**, *22*, 2424–2432.

(51) Stellwagen, E.; Lu, Y.; Stellwagen, N. C. *Biochemistry* **2003**, *42*, 11745–11750.

(52) Manning, G. S. *Q. Rev. Biophys.* **1978**, *11*, 179–246.

(53) Alexander, S.; Chaikin, P. M.; Grant, P.; Morales, G. J.; Pincus, P.; Hone, D. *J. Chem. Phys.* **1984**, *80*, 5776–5781.

(54) Borukhov, I. *J. Polym. Sci.: Part B* **2004**, *42*, 3598–3615.

(55) Cantor, C.; Schimmel, P. *Biophysical Chemistry*; W.H. Freeman: New York, 1980.

(56) All species subjected to electrokinetic measurement were made from DNA oligomers with 23 phosphodiester bonds, except for Agn:12C, which has 26.
(57) Ritchie, C. M.; Johnsen, K. R.; Kiser, J. R.; Antoku, Y.; Dickson, R. M.; Petty, J. T. *J. Phys. Chem. C* **2007**, *111*, 175–181.
(58) Mitrić, R.; Ptersen, J.; Kulesza, A.; Bonačić-Koutecký, V.; Tabarin, T.; Compagnon, I.; Antoine, R.; Broyer, M.; Dugourd, P. *Chem. Phys.* **2008**, 343.
(59) Kulesza, A.; Mitrić, R.; Bonačić-Koutecký, V.; Bellina, B.; Compagnon, I.; Broyer, M.; Antoine, R.; Dugourd, P. *Angew. Chem. Int. Ed.* **2011**, *50*, 878–881.
(60) Khurana, T. K.; Santiago, J. G. *Anal. Chem.* **2008**, *80*, 279–286.
(61) *O-063190 Alexa Fluor Dye Selection Guide*; Invitrogen Corp.: Carlsbad, CA, 2005.
(62) Nitsche, J. M.; Chang, H.-C.; Weber, P. A.; Nicholson, B. J. *Biophys. J.* **2004**, *86*, 2058–2077.